

Richard A. Snay\*, Jarir Saleh, and Chris F. Pearson

# Improving TRANS4D's model for vertical crustal velocities in Western CONUS

<https://doi.org/10.1515/jag-2018-0010>

Received March 26, 2018; accepted April 26, 2018

**Abstract:** The “Transformations in Four Dimensions” (TRANS4D) software was developed to enable geospatial professionals and others to transform 3-D positional coordinates referred to one date to corresponding positional coordinates referred to another date. For this purpose, TRANS4D incorporates 3-D crustal velocity models for most of the United States and Canada. In this report, an improved model for the vertical velocity field of that part of the conterminous United States that resides west of longitude 107°W is introduced. A new estimation process was employed so that this newer velocity field would have a spatial resolution of  $0.0625^\circ \times 0.0625^\circ$  in latitude and longitude, whereas the spatial resolution of TRANS4D's previous model for this area was  $0.25^\circ \times 0.25^\circ$ . The realized improvements benefited from the inclusion of repeated geodetic data at approximately 1300 new locations and from the longer time spans of repeated geodetic data at other locations. After removing that part of the current vertical velocity field due to the glacial isostatic adjustment associated with the Last Glacial Maximum, features of the remaining vertical velocity field are discussed in terms of ongoing geophysical processes. These processes include subduction in the Pacific Northwest, uplift along the San Andreas Fault System, and subsidence due to groundwater extraction in California's Central Valley. They also include uplift within both the Yellowstone Caldera and the Long Valley Caldera, uplift near Hebgen Lake in Montana, and subsidence near Lassen Peak Volcano in California.

**Keywords:** vertical crustal motion, tectonic deformation, glacial isostatic adjustment, groundwater extraction

## 1 Introduction

Snay et al. [37] introduced a prototype of the TRANS4D software where TRANS4D is short for “Transformations in

\*Corresponding author: Richard A. Snay, National Geodetic Survey (retired), Montgomery Village, Maryland, USA, e-mail: rssnay@aol.com

Jarir Saleh, National Geodetic Survey, Silver Spring, Maryland, USA, e-mail: Jarir.Saleh@noaa.gov

Chris F. Pearson, Surveying Department, University of Otago, Dunedin, New Zealand, e-mail: chris.pearson@otago.ac.nz

Four Dimensions”. TRANS4D is being developed to enable geospatial professionals and others to transform three-dimensional (3-D) positional coordinates across time and between spatial reference frames. Among other features, TRANS4D incorporates numerical models for 3-D crustal velocities for the conterminous United States (CONUS), and most of Alaska and Canada. These models are encoded into the software by designating a collection of 2-D rectangular grids in latitude and longitude, where each grid spans a region that is bounded by maximum and minimum latitudes and longitudes. For each grid node, the software stores a 3-D velocity that had been previously estimated, primarily from repeated geodetic data. The software computes velocities at other locations within the gridded regions via bilinear interpolation of the velocities at the four nodes that define the grid cell encompassing the location of interest.

### 1.1 The study area

In [37], numerical 3-D velocity models were developed for six gridded regions that, in combination, span CONUS and most of Alaska and Canada. This study will focus on refining the vertical component of the 3-D velocity model for only one of these six regions, the Western CONUS region, which extends in latitude from 31°N to 49°N and in longitude from 107°W to 125°W (Figure 1). In [37], the vertical component of the 3-D velocity model for Western CONUS was developed for a 2-D grid whose nodes have a  $0.25^\circ \times 0.25^\circ$  spacing in latitude and longitude. In this study, a vertical velocity model for Western CONUS is developed for a 2-D grid whose nodes have a  $0.0625^\circ \times 0.0625^\circ$  spacing. This improved spatial resolution has been made possible thanks to the availability of repeated geodetic data at approximately 1300 new locations and to longer time spans of repeated geodetic data at other locations. In particular, this study includes some GNSS data observed as recently as mid-2017, whereas all of the GNSS data used by Snay et al. [37] were observed in 2013 or earlier. Also, techniques for deriving crustal velocities from repeated geodetic data have greatly improved. These various improvements are due to contributions by numerous institutions and individuals. Note that an improved model for the horizontal velocities occurring in western CONUS was also developed, but

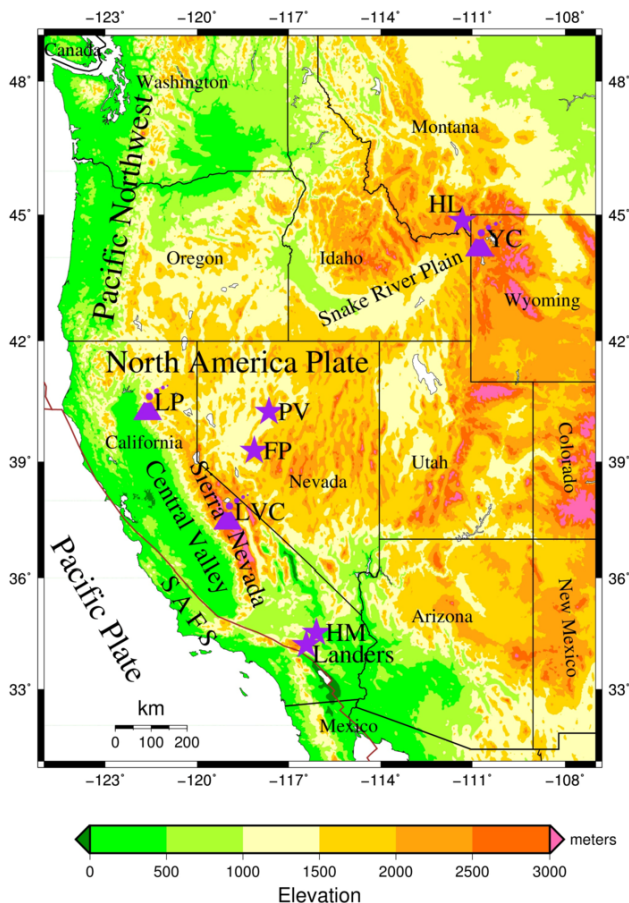


**Figure 1:** Selected features and topography of Western CONUS. Brown line segments approximate plate boundaries including the San Andreas Fault System (SAFS) in central and southern California. Purple volcanic symbols designate selected magmatic features including Lassen Peak (LP), Yellowstone Caldera (YC), and Long Valley Caldera (LVC). Purple stars designate selected earthquakes including Hebgen Lake (HL)/1959/M7.3, Pleasant Valley (PV)/1915/M7.2, Fairview Peak (FP)/1954/M7.1, Hector Mine (HM)/1999/M7.1, and Landers/1992/M7.3.

this new horizontal model is not discussed here because its velocities differ only slightly from the corresponding horizontal velocities generated by the model of Snay et al. [37].

Several geophysical phenomena contribute to the vertical motion that has occurred in Western CONUS. These phenomena include: (a) land subsidence due to the withdrawal of underground fluids (water, petroleum, and gas), (b) tectonic motion such as that associated with the subduction of the Juan de Fuca plate beneath the North America plate, (c) volcanic activity including the intrusion of magma into subterranean chambers associated with either the Yellowstone Caldera or the Long Valley Caldera, (d) postseismic deformation, and (e) the glacial isostatic adjustment (GIA) associated with the past melting of the

ice fields and glaciers that were formed more than 19,000 years ago during the Last Glacial Maximum. Each of these phenomena will be discussed in some detail in this report. The vertical motion associated with these phenomena can exhibit both spatial and temporal variations. The modeling process to be presented here, however, addresses only the spatial variations.

## 1.2 Overview of the velocity modeling process

The employed velocity modeling process is a two-step procedure that uses previously derived vertical velocities at specific sites (for example, velocities derived from repeated geodetic observations) to estimate vertical velocities throughout a specific region of study, in this case the Western CONUS region. For the purpose of convenience, such previously derived site velocities shall be referred to as “observed” velocities.

For the first step (to be called Step A), a preliminary model of the vertical velocity field is specified. This preliminary model may be imported from a previous study. Alternatively, this preliminary model may be developed by using mathematical equations to characterize velocities in terms of relevant parameters. For example, all or part of the preliminary velocity field may be characterized by steady slip on each of several geologic fault segments, whereby for each fault segment, a slip rate vector is specified together with the dimensions, location, and orientation defining this fault segment.

For the second step (to be called Step B), a residual vertical velocity is calculated for each “observed” vertical velocity by subtracting from this observed velocity its corresponding vertical velocity yielded by the preliminary velocity model of Step A. Then an interpolation process is applied to the set of residual vertical velocities to estimate an incremental vertical velocity for designated points located within the region. These incremental vertical velocities (whose values may be either positive or negative) are then added to their corresponding vertical velocities produced in Step A to generate revised vertical velocities for locations within the region.

For a given study, the revised model from Step B may be considered to be the “final” velocity model. However, the nature of this final model, perhaps together with some additional information, may produce insights as to how the underlying vertical velocity field may be better represented by an improved model, whereby the two-step process may be iterated starting with producing a new preliminary model. In subsequent sections of this publication,

the employed two-step velocity modeling process will be described in greater detail.

Section 2 of this paper describes the geodetic data used to produce the new vertical velocity model for Western CONUS, and Section 3 discusses the adopted preliminary vertical velocity model involved in the implementation of Step A. Section 4 presents the mathematics associated with the interpolation process involved in Step B. Section 4 also presents the newly derived vertical velocity model that has been encoded in TRANS4D (version 0.2). Section 5 discusses standard deviations associated with the increment to the preliminary vertical velocities, and Section 6 reveals how vertical velocities might look if the currently occurring vertical motion were modified so as to remove the current vertical motion due solely to the glacial isostatic adjustment (GIA) following the melting of the ice fields that formed during the Last Glacial Maximum. Section 7 discusses relationships between estimated vertical velocities and some geophysical processes that occur in Western CONUS, both natural and anthropogenic. Finally, Section 8 summarizes the contents of this report.

## 2 Geodetic data

The new vertical velocity model for Western CONUS has been formulated, in part, by using 3-D velocity vectors derived from repeated GNSS observations, repeated trilateration observations, and repeated very-long-baseline-interferometry (VLBI) observations at approximately 3300 geodetic-quality reference stations. This new velocity model has also been formulated by using vertical velocities derived from repeated leveling data at 598 geodetic-quality reference stations located near the Pacific Coast of Oregon and northern California [10]. In addition, this new velocity model has also been developed by using vertical velocities derived from repeated satellite radar altimetry at 690 points located in California's Central Valley [24].

### 2.1 Velocity vectors derived from GNSS, trilateration, and/or VLBI data

Geodetically derived 3-D velocity vectors were obtained from nine separate data sets produced by multiple institutions and researchers. In many cases, a velocity vector found in one data set may have been computed from essentially the same geodetic data used to compute a velocity vector found in another data set. The nine data sets include the following:

*The International GNSS Service (IGS) data set based on continuous GNSS data observed between 2 January 1994 (GPS Week 730) and 15 April 2017 (GPS Week 1944) at more than 1500 IGS-affiliated stations distributed around the world ([ftp://cddis.gsfc.nasa.gov/gps/products/1944/IGS17P15\\_all.ssc.Z](ftp://cddis.gsfc.nasa.gov/gps/products/1944/IGS17P15_all.ssc.Z)). This IGS data set is based on time series of daily positional coordinates derived from both GPS and GLONASS data. The time series were developed collaboratively by merging nine separate solutions for daily coordinates, where each of these nine solutions had been developed by a different institution. The IGS updates its solution on a weekly basis. These IGS velocities are referred to the IGS14 reference frame which represents the GNSS realization of the International Terrestrial Reference Frame of 2014 (ITRF2014) [2, 32]. (Note: IGS considers IGS14 velocities to be essentially equivalent to ITRF2014 velocities in the sense that there are no known systematic differences between these two sets of velocities, although IGS14 velocities may differ from their corresponding ITRF2014 velocities at individual stations.)*

*A data set produced by the University of Nevada, Reno (UNR) which provides estimated IGS08-consistent velocities for more than 10,400 continuous GPS stations distributed around the world. The UNR solution is updated weekly with the latest being available at <http://geodesy.unr.edu>. The UNR solution for 2 May 2017 was downloaded for this study. This data set is of special interest because it utilizes the MIDAS algorithm [6] to estimate velocities from coordinate time series in a manner that is both automated and resistant to common problems such as step discontinuities, outliers, seasonality, skewness, and heteroscedasticity. (Note: the IGS08 reference frame [33] is the GNSS realization of ITRF2008 [1].)*

*A GAGE (Geodesy Advancing Geosciences and Earth-Scope) data set which provides IGS08-consistent velocities for more than 2600 continuous GPS stations including those contained in UNAVCO's Plate Boundary Observatory (PBO), as well as those contained in several related networks [20]. While the PBO stations are distributed primarily throughout the United States, other stations in this GAGE data set provide a more global distribution. The GAGE solution is updated approximately once per year with the latest velocity estimates being available at [ftp://data-out.unavco.org/pub/products/velocity/pbo\\_final\\_igs08.vel](ftp://data-out.unavco.org/pub/products/velocity/pbo_final_igs08.vel). The GAGE data set released in December 2016 was downloaded for this study.*

*A MEaSUREs (Making Earth System Data Records for Use in Research Environments) data set that the Jet Propulsion Laboratory and Scripps Orbit and Permanent Array Center jointly produced [8]. The downloaded MEaSUREs*

**Table 1:** Estimated values for the transformation parameters from the IGS set of velocities to each of the other sets of velocities, together with other information.

Data Set	IGS	UNR	NGS	SCEC	McCaffrey	NRCan	UAF	MEaSUREs	GAGE
Total number of stations	1598	10,422	1375	807	971	500	910	2657	2670
Stations in other data sets	1546	3686	1363	251	337	471	337	2518	2664
Time span of data	1994–2017	1994–2017	1993–2011	1970–2004	1993–2011	1994–2011	1992–2013	1995–2017	1994–2016
Original reference frame	IGS14	IGS08	IGS08	SNARF 1.0 <sup>(a)</sup>	SNARF 2.0 <sup>(b)</sup>	IGS08	IGS08	IGS08	IGS08
$\dot{T}_x$ (mm/yr)	0.00	0.06	0.06	0.91	-0.31	0.24	0.41	0.01	-0.45
$\dot{T}_y$ (mm/yr)	0.00	0.04	0.02	-4.38	0.06	0.14	-0.21	-0.05	-0.75
$\dot{T}_z$ (mm/yr)	0.00	-0.10	-0.19	-7.87	-3.34	-0.44	-0.39	-0.16	-0.50
$\dot{R}_x$ (nrad/yr)	0.00	0.00	0.00	1.51	0.57	0.01	0.02	0.01	0.11
$\dot{R}_y$ (nrad/yr)	0.00	-0.01	0.00	-3.20	-3.09	0.01	0.05	0.00	-0.11
$\dot{R}_z$ (nrad/yr)	0.00	0.01	0.00	-0.24	-0.45	0.05	0.00	0.00	0.05
$\dot{S}$ (ppb/yr)	0.00	0.05	0.05	0.44	0.29	0.12	0.03	0.04	0.01

<sup>(a)</sup>See [5].<sup>(b)</sup>See [19].

data set provides IGS08-consistent velocities for more than 2600 continuous GPS stations distributed around the world. This data set is regularly updated, and the latest velocity estimates are available at <http://geoapp03.ucsd.edu/gridsphere/gridsphere>. The data set available on 24 April 2017 was downloaded for this study.

The remaining five data set are the same as those used by Snay et al. [37]. They include:

- The data set published by McCaffrey et al. [25] which provides velocities for many continuous GPS stations, as well as for many episodically monitored GPS stations, located mainly in and around northwestern CONUS;
- The Southern California Earthquake Center (SCEC) data set known as “Crustal Motion Model Four” [35] which provides estimated velocities for continuous GPS stations, as well as episodically monitored stations, located mainly in and around southern California; the SCEC data set also includes VLBI data observed under the auspices of NASA and trilateration data observed under the auspices of the U.S. Geological Survey;
- The U.S. National Geodetic Survey (NGS) data set that provides velocities for continuous GPS stations in the NGS-affiliated Continuously Operating Reference Station network [17];
- The Natural Resources Canada (NRCan) data set for velocities at both continuous and episodically monitored GPS stations located in and around Canada [14];

- An unpublished data set produced by the University of Alaska Fairbanks (UAF) which provides velocities for continuous GPS stations and episodically monitored GPS stations in and around Alaska.

Using the combination process described in Appendix A of Snay et al. [37], the geodetically derived velocities from these nine data sets were employed to estimate a single 3-D IGS14 velocity for each of approximately 12,500 distinct geodetic stations. Of these stations, approximately 3300 reside either in the Western CONUS region or within approximately 50 km of this region. The remaining stations span the globe. Velocities at stations located around the world were included in the combination process to more accurately estimate the seven parameters required for each of the nine data sets to transform its velocities from their associated reference frame to the IGS14 reference frame. Actually, a set of seven parameters is needed for each of only eight of the data sets because the velocities of the IGS solution are already referred to IGS14. The seven parameters include three translation rates ( $\dot{T}_x$ ,  $\dot{T}_y$ ,  $\dot{T}_z$ ), three rotation rates ( $\dot{R}_x$ ,  $\dot{R}_y$ ,  $\dot{R}_z$ ), and a scale change rate ( $\dot{S}$ ). Here, the subscripts – X, Y, Z – pertain to the three axes of a traditional right-handed Earth-centered-Earth-fixed Cartesian coordinate system with the Z-axis approximating Earth’s axis of rotation and the X-axis piercing Earth’s equator near 0° longitude. Table 1 presents resulting estimates for the values of these parameters. Although the velocities for six of the input data sets are nominally referred to IGS08, a separate set of seven parameters was es-

timated for each of these six data solutions in anticipation of possible discrepancies among these six data sets. See [37] for additional information about the employed combination process.

In this publication, velocity estimates contained in the nine data sets are referred to as “stage-1” velocities; and the velocity estimates produced via the combination process are referred to “stage-2” velocities. In subsequent sections of this publication, a two-step process to model the stage-2 velocities is described. The resulting model provides 3-D velocities as a function of latitude and longitude. These modeled velocities are referred to as “stage-3” velocities. Stage-3 velocities correspond to the velocities encoded into the TRANS4D software.

The standard deviation assigned to a stage-2 velocity component (east, north, up) of a geodetic station equals the minimum value of the reported standard deviations, pertaining to this velocity component, among all of the stage-1 velocities at this station with the following restrictions: (1) the standard deviation of a stage-2 horizontal velocity component cannot be smaller than 0.2 mm/yr and (2) the standard deviation of a stage-2 vertical velocity component cannot be smaller than 0.3 mm/yr. The standard deviation of a stage-2 velocity component was assigned in this way because the various stage-1 velocities for a station are based upon very similar sets of geodetic data and thus do not represent independent estimates. Unfortunately, adopting the minimum of the estimated standard deviations may be problematic if some institutions systematically underestimate the standard deviations for their estimated velocities.

## 2.2 Vertical velocities derived from leveling data

Burgette et al. [10] used leveling surveys performed by NOAA’s National Geodetic Survey in the 1930s, in 1941, and in the 1980s to derive vertical velocities at 598 geodetic-quality reference stations (commonly referred to as benchmarks). In combination, the stations in the repeated leveling surveys form four strands (see Figure 2). The longest strand traverses from north to south along the entire length of Oregon’s coast and along approximately the northernmost 20 km of California’s coast. Each of the other three strands traverses eastward from this north-south strand at a different latitude and for more than 50 km into Oregon’s interior. These authors also used rates of relative sea level change measured at six NOAA tide gauge stations, located in this same area, to calibrate their derived vertical velocities. The nominal standard error of their derived

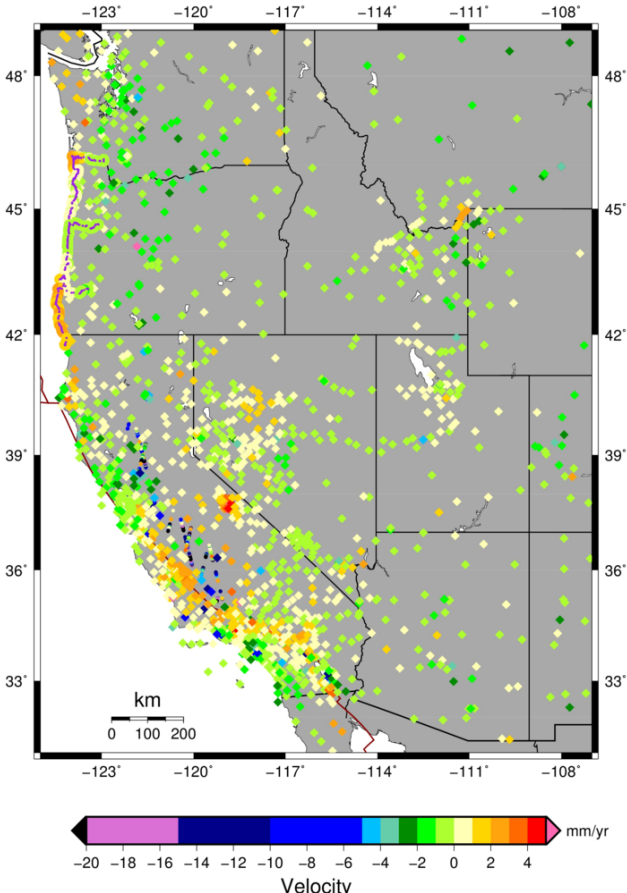


**Figure 2:** IGS14 vertical velocities derived from repeated geodetic data. Diamonds identify velocities derived from GNSS, trilateration, or VLBI data. Small purple dots near the Oregon coast designate leveling data locations, and the larger dots behind these purple dots identify velocities derived from the leveling data. The small dots in California’s Central Valley identify velocities derived from satellite radar altimetry. Velocities with standard deviations exceeding 1.0 mm/yr are not presented unless they were derived from altimetry data.

vertical velocities equals approximately 0.4 mm/yr at the majority of the 598 sites. Unfortunately, vertical velocities derived from leveling data differ in nature from vertical velocities derived from GNSS data, and thus some care needs to be employed when combining these two types of velocities, as is discussed in Appendix A.

## 2.3 Vertical velocities derived from satellite radar altimetry

A satellite-borne radar altimeter measures the two-way travel time of a radar pulse. This travel time is used to compute the distance between the satellite and the Earth’s sur-

face, and after computing the precise orbit of the satellite, the height of the surface can be computed [24]. Then, by using multiple heights measured at a common point on a ground track that has been retraced many times during the span of several years, the vertical velocity at this point may be estimated. Hwang et al. [24] employed this technology to estimate vertical velocities at points located in California's Central Valley, as well as points located in Taiwan and China. They have since provided some of their California velocities for use in this study. Their provided velocities greatly augment the relatively few GNSS-derived velocities existing in California's Central Valley, where vertical velocities vary significantly as a function of location. In particular, Dr. Hwang and his colleagues provided vertical velocities (and their respective standard deviations) at approximately 690 sites. These velocities were derived from radar altimetry involving the ENVISAT satellite that is sponsored by the European Space Agency. These ENVISAT measurements span the interval from July 2002 to October 2010. See [24] for additional information as to how they processed their altimetry data.

The provided velocities are spaced at  $\sim$ 1-km intervals within each of several ground tracks, as depicted in Figure 2. The standard deviations associated with these estimated velocities vary from a few mm/yr to several 10s of mm/yr, with better precision found within areas of flatter terrain. Before including these velocities into this study, their values were uniformly increased by 3.5 mm/yr to make them more compatible with IGS14 vertical velocities derived from GNSS data at stations located within 1 km of an ENVISAT ground track.

### 3 Step A: Specifying a preliminary velocity model

For this study, the preliminary model for the vertical velocities occurring in and around Western CONUS equals the vertical velocity model encoded in the TRANS4D (version 0.1) software (Figure 3). The development of this velocity model is described in [37]. It will be assumed that deviations from these preliminary vertical velocities vary rather smoothly as a function of latitude and longitude, and hence these deviations may be adequately estimated via an interpolation process. In the next section an interpolation process is introduced. This interpolation process differs from kriging [16], but the two processes are similar in several ways.

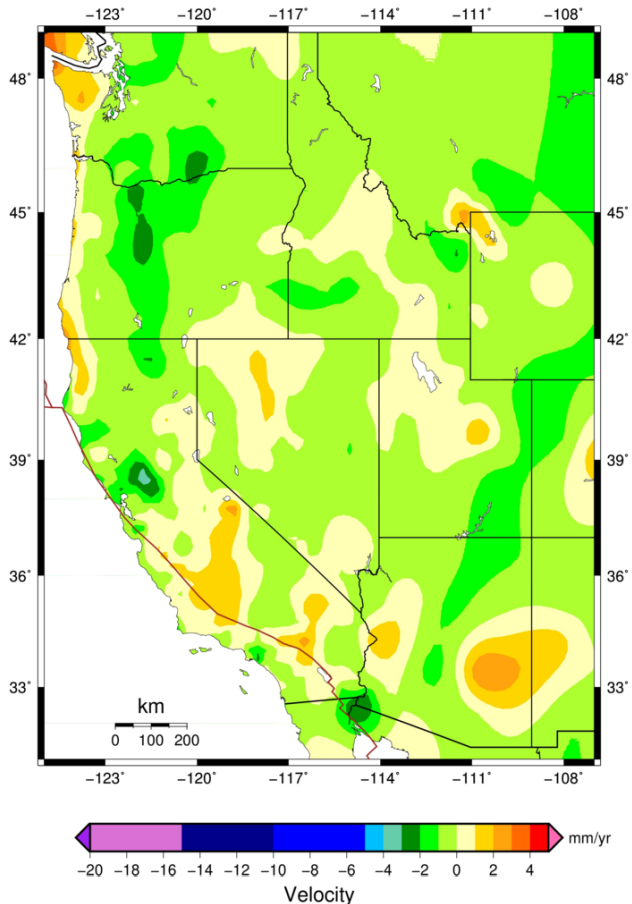


**Figure 3:** IGS08 vertical velocities from the model encoded in TRANS4D (version 0.1). These velocities served as the preliminary velocities in the estimation process to obtain improved vertical velocities.

### 4 Step B: Interpolating residual velocities

To start Step B, a residual vertical velocity for each “observed” vertical velocity is calculated by subtracting from this observed velocity its corresponding preliminary velocity. It will be assumed that the covariance between any two of the residual velocities varies essentially as a function of the distance between the locations. That is, if  $v_i$  and  $v_j$  denote the residual vertical velocities at locations  $i$  and  $j$ , respectively; then there is a function  $C(d)$  such that

$$\text{Cov}(v_i, v_j) = C(d_{ij}) \quad (1)$$

for all possible locations  $i$  and  $j$  contained in the study area. Here,  $\text{Cov}(v_i, v_j)$  denotes the covariance between  $v_i$  and  $v_j$ , and  $d_{ij}$  denotes the distance between location  $i$  and location  $j$ .

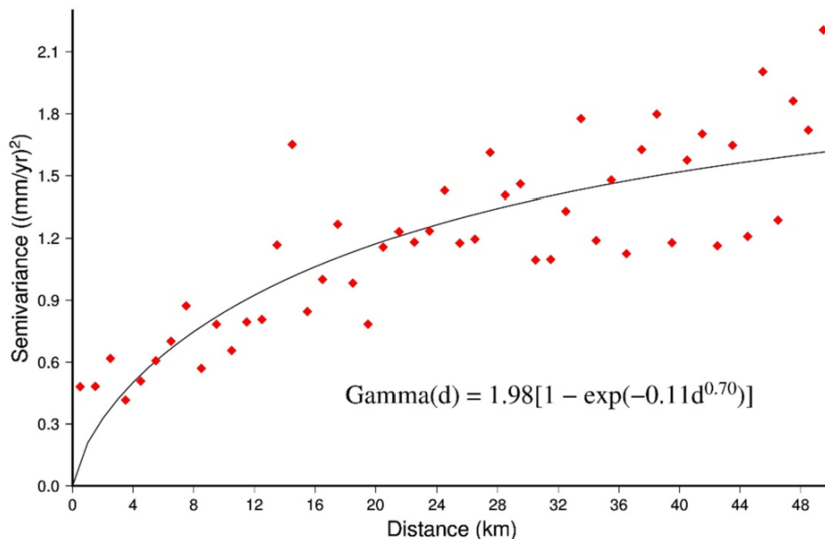


**Figure 4:** Semivariogram: semivariance as a function of distance.

Under the condition of second-order stationarity (spatially constant mean and variance of the residual velocity field within the study area), which is justified due to the removal of significant velocity trends in step A, the function  $C(d)$  is related to another function  $\Gamma(d)$  by the equation

$$C(d) = C(0) - \Gamma(d). \quad (2)$$

$\Gamma(d)$  is called the semivariogram function.

The value of  $C(0)$  may be estimated by the equation

$$C(0) = \sum_{i=1}^N (v_i - m)^2 / (N - 1) \quad (3)$$

where  $m$  denotes the mean velocity, that is,

$$m = \sum_{i=1}^N v_i / N \quad (4)$$

Here  $v_i$  denotes the residual vertical velocity at location  $i$ , and  $N$  denotes the number of residual vertical velocities being considered.

The function  $\Gamma(d)$  may be approximated for the interval  $\delta_1 < d < \delta_2$  by considering all pairs of locations ( $i$  and  $j$ ) with residual vertical velocities  $v_i$  and  $v_j$  and such that the distance between location  $i$  and location  $j$  is greater than  $\delta_1$  and less than  $\delta_2$  and then computing

$$\Gamma(d) \approx \sum_{i < j}^{N(d)} (v_i - v_j)^2 / 2N(d) \quad (5)$$

Here  $N(d)$  denotes the number of unique pairs of locations such that the distance between a pair's locations falls within the given interval.

The collection of approximations to  $\Gamma(d)$  for the various intervals may then be fitted to an analytical function.

The choice of the analytical function is somewhat subjective. In this study, functions of the form

$$\Gamma(d) = C(0)[1 - \exp(-\alpha d^\beta)] \quad (6)$$

were considered where  $\alpha$  and  $\beta$  represent constants to be estimated from the collection of approximations to  $\Gamma(d)$ .

For estimating the parameters involved in the previous equations, only those “observed” vertical velocities having standard deviations less than 1.0 mm/yr were considered. The residuals to these vertical velocities yielded  $m = -0.11$  mm/yr and  $C(0) = 1.98$  (mm/yr)<sup>2</sup>. The fact that the estimated value of  $m$  is rather small indicates that the previous vertical velocity model for Western CONUS (that is, the velocity model encoded in TRANS4D (version 0.1)) is accurate on average. However, the fact that the estimated value of  $C(0)$  is rather large reveals that this previous model neglected many significant short wavelength features.

An average value for  $\Gamma(d)$  was estimated for each km-wide interval  $[d - 0.5, d + 0.5]$  for  $d = 0.5, 1.5, 2.5, \dots, 49.5$  kilometers. The diamonds shown in Figure 4 represent these estimated values. The curve shown in Figure 4 represents the best fitting curve in the form of Equation (6). For this curve,  $\alpha = 0.11$  and  $\beta = 0.70$ . The large scatter of the diamonds about this curve indicates that there are various characteristics of the vertical velocity field that were not adequately addressed when developing TRANS4D (version 0.1). For example, some of these short wavelength features most likely correspond to large subsidence rates that vary significantly over short distances, especially those subsidence rates associated with groundwater extraction.

Having developed a semivariogram function  $\Gamma(d)$ , the incremental vertical velocity (denoted  $v_p$ ) at an arbitrary location (denoted  $p$ ) may be estimated via a weighted least squares process involving  $M$  observations and  $M$  stochastic constraints, where  $M$  denotes the number of geodetic stations (with “observed” velocities) that are located within a specified distance of  $p$ . This incremental vertical velocity is to be added to the preliminary vertical velocity at  $p$  (from Step A) to obtain the final vertical velocity at  $p$ . Each of the  $M$  observations is of the form

$$v_i = b_i + e_i \quad (7)$$

where  $b_i$  denotes the residual vertical velocity at geodetic station  $i$ , and  $e_i$  denotes the (yet unknown but zero-mean) random error in this measurement for  $i = 1, 2, \dots, M$ . Each of the  $M$  stochastic constraints, or pseudo-observations, is of the form

$$v_p - v_i = 0 + e_{i+M} \quad (8)$$

where  $e_{i+M}$  denotes a (yet unknown but zero mean) random error for  $i + M = 1 + M, 2 + M, \dots, 2M$ .

These  $M$  constraints are correlated with one another, and their associated weight matrix equals  $Q^{-1}$  where

$$Q = \begin{vmatrix} Var(v_p - v_1) & Cov[(v_p - v_1), (v_p - v_2)] \\ Cov[(v_p - v_2), (v_p - v_1)] & Var(v_p - v_2) \\ \vdots & \vdots \\ Cov[(v_p - v_M), (v_p - v_1)] & Cov[(v_p - v_M), (v_p - v_2)] \\ \dots & Cov[(v_p - v_1), (v_p - v_M)] \\ \dots & Cov[(v_p - v_2), (v_p - v_M)] \\ \dots & \vdots \\ \dots & Var(v_p - v_M) \end{vmatrix} \quad (9)$$

For the diagonal elements of  $Q$ ,

$$\begin{aligned} Var(v_p - v_i) &= Var(v_p) + Var(v_i) - 2Cov(v_p, v_i) \\ &= C(0) + C(0) - 2C(d_{p,i}) \\ &= 2\Gamma(d_{p,i}) \end{aligned} \quad (10)$$

where  $d_{p,i}$  denotes the distance between  $p$  and the  $i^{\text{th}}$  geodetic station.

For the off-diagonal elements,

$$\begin{aligned} Cov[(v_p - v_i), (v_p - v_j)] &= Var(v_p) - Cov(v_p, v_i) - Cov(v_p, v_j) + Cov(v_i, v_j) \\ &= C(0) - C(d_{p,i}) - C(d_{p,j}) + C(d_{i,j}) \\ &= \Gamma(d_{p,i}) + \Gamma(d_{p,j}) - \Gamma(d_{i,j}). \end{aligned} \quad (11)$$

The set of  $M$  observations and  $M$  constraints may be expressed as the matrix equation

$$AV = L + E \quad (12)$$

where

$$V_{(M+1) \times 1} = [v_p, v_1, v_2, \dots, v_M]^T \quad (13)$$

$$L_{2M \times 1} = [b_1, b_2, \dots, b_M, 0, 0, 0, \dots, 0]^T \quad (14)$$

$$E_{2M \times 1} = [e_1, e_2, \dots, e_{2M}]^T \quad (15)$$

and

$$A_{2M \times (M+1)} = \begin{vmatrix} 0 & 1 & 0 & 0 & \dots & 0 \\ 0 & 0 & 1 & 0 & \dots & 0 \\ 0 & 0 & 0 & 1 & \dots & 0 \\ \vdots & \vdots & \vdots & \vdots & \dots & \vdots \\ 0 & 0 & 0 & 0 & \dots & 1 \\ 1 & -1 & 0 & 0 & \dots & 0 \\ 1 & 0 & -1 & 0 & \dots & 0 \\ 1 & 0 & 0 & -1 & \dots & 0 \\ \vdots & \vdots & \vdots & \vdots & \dots & \vdots \\ 1 & 0 & 0 & 0 & \dots & -1 \end{vmatrix} \quad (16)$$

The least squares solution for the elements of  $V$  corresponds to the one that minimizes the quantity  $E^T \Sigma^{-1} E$  where

$$\Sigma_{2M \times 2M} = \begin{vmatrix} W & [0] \\ [0] & Q \end{vmatrix} \quad (17)$$

Here  $W$  is an  $M \times M$  diagonal matrix whose  $i^{\text{th}}$  diagonal element equals  $\sigma_i^2$  where  $\sigma_i$  denotes the standard deviation of  $b_i$ , and  $[0]$  is the  $M \times M$  matrix whose elements all equal zero. Note that the standard deviation of  $b_i$  is set equal to the standard deviation of the “observed” velocity of which  $b_i$  is the residual velocity.

The least squares estimate is given by the equation

$$V = (A^T \Sigma^{-1} A)^{-1} A^T \Sigma^{-1} L \quad (18)$$

from which an estimate for  $v_p$  may be obtained.

The covariance matrix for the estimates of  $V$  is given by the equation

$$Cov(V) = (A^T \Sigma^{-1} A)^{-1} \quad (19)$$

from which the standard deviation for the estimate of  $v_p$  may be obtained.

Note that for the special case,  $M = 1$ , the estimate of  $v_p$  equals  $b_1$  and the standard deviation of this estimate equals  $[\sigma_1^2 + 2\Gamma(d_{p,1})]^{0.5}$ .

Figure 5 displays the incremental vertical velocity field obtained by applying the described process to estimate the increment at each node of a  $0.0625^\circ \times 0.0625^\circ$  grid that spans the Western CONUS region. The incremental vertical velocity at each non-nodal location within Western CONUS

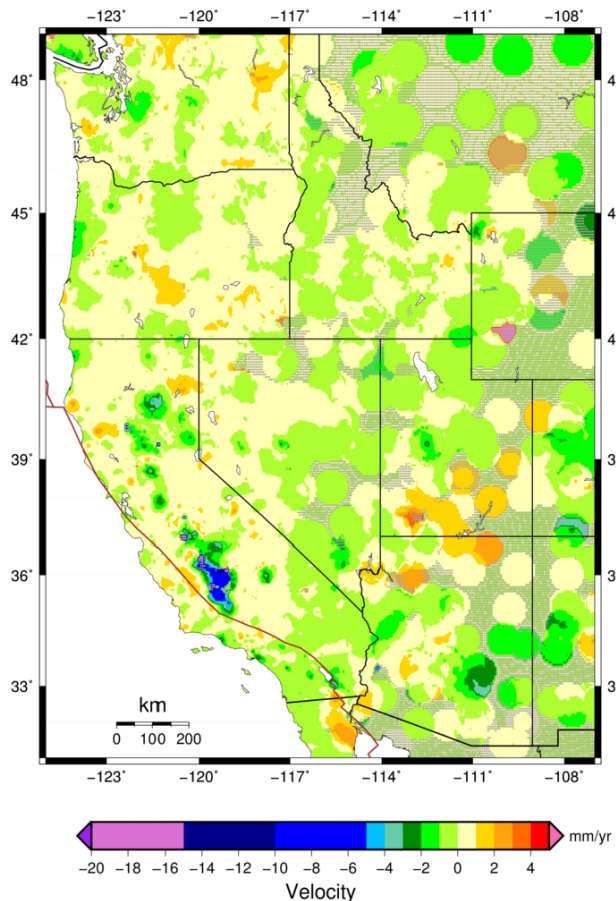


**Figure 5:** Estimated increments to the IGS08 vertical velocities encoded into TRANS4D (version 0.1). These increments were added to their corresponding IGS08 vertical velocities to generate the corresponding IGS14 vertical velocities encoded into TRANS4D (version 0.2). Gray screening identifies areas where these estimated increments have standard deviations exceeding 2.0 mm/yr.

was then estimated via bilinear interpolation using the incremental vertical velocities of the four nodes defining the grid cell containing this non-nodal location.

To estimate the incremental vertical velocity at a grid node, residual vertical velocities were employed from only those geodetic data points located within 25 km of this node. However, if fewer than four such data points existed within 25 km, then the incremental vertical velocity was estimated using residual vertical velocities from all geodetic data points located within 50 km of this node. In the case where no geodetic data points are located within 50 km, then the incremental vertical velocity at the node was set equal to 0.0 mm/yr with a standard deviation of 5.0 mm/yr.

Figure 6 displays the new vertical velocity field for Western CONUS as incorporated into TRANS4D (version 0.2). This new velocity field was obtained by adding the in-

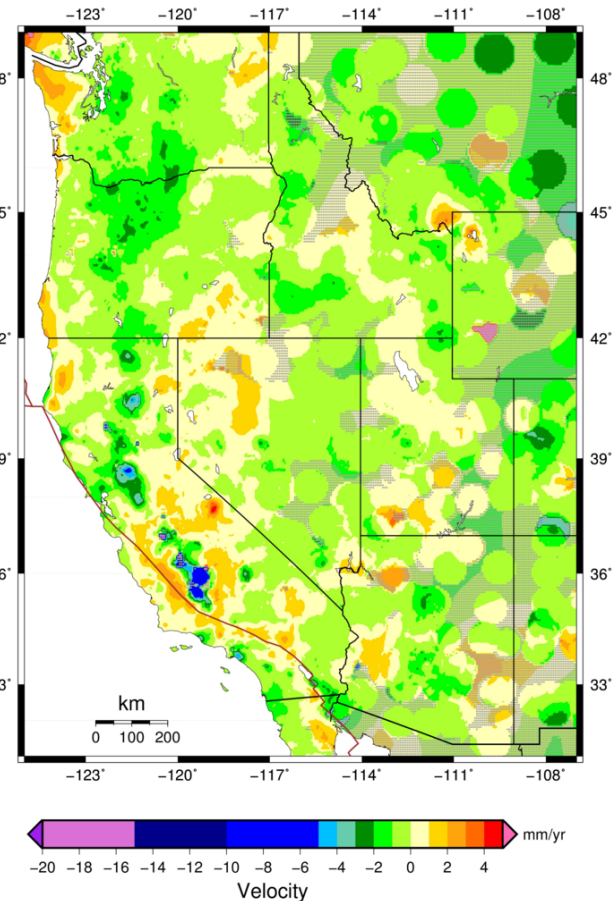


**Figure 6:** IGS14 vertical velocities from the new model encoded in TRANS4D (version 0.2). Gray screening identifies areas where increments to the IGS08 vertical velocities from TRANS4D (version 0.1) have standard deviations exceeding 2.0 mm/yr.

cremental vertical velocity field presented in Figure 5 to the preliminary vertical velocity field portrayed in Figure 3. Recall that the preliminary vertical velocity field equals that yielded by TRANS4D (version 0.1).

## 5 Standard deviations of velocities

The estimation process of Step B provides an estimated standard deviation for the incremental velocity at each grid node. The standard deviations at other locations were approximated from those at the grid nodes via bilinear interpolation. Figure 7 presents the standard deviations for the estimated incremental vertical velocities.

As expected, the magnitudes of these standard deviations reflect the spatial distribution of the available geodetic observations. Hence, these standard deviations are generally small along the Pacific Coast of Western

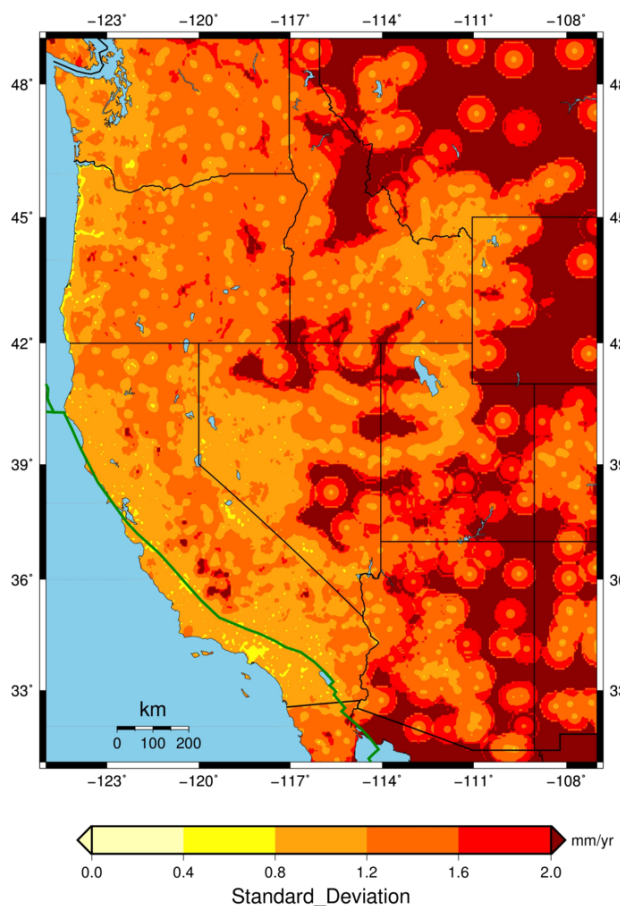


**Figure 7:** Standard deviations of the vertical-velocity increments presented in Figure 5.

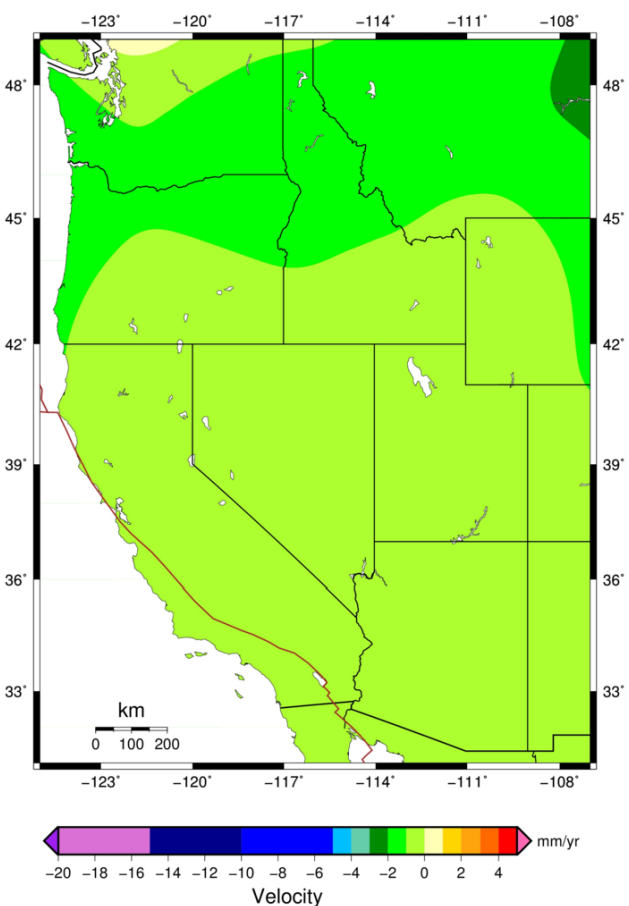


**Figure 8:** Present-day vertical velocities due to the GIA associated with the past melting of the ice fields that formed during the Last Glacial Maximum. These IGS08 velocities were obtained using the ICE-6G\_C(VM5a) model.

CONUS where numerous geodetic observations have been performed over the years to address earthquake-related concerns. In addition, standard deviations for the incremental vertical velocities are especially small along the Pacific Coast of Oregon thanks to the availability of repeated leveling data of good quality. Also, standard deviations are generally small in highly populated areas and they are generally large in sparsely populated areas, because the spatial density of geodetic data often reflects local population density.

It should be noted that the vertical velocities portrayed in Figures 5 and 6 and the standard deviations portrayed in Figure 7 are all functionally related to the adopted semi-variogram function  $\Gamma(d)$  and its accuracy.

## 6 Removing GIA-related motion

The vertical velocities occurring throughout Western CONUS include a contribution due to the glacial isostatic

adjustment (GIA) associated with past melting of the ice fields that formed more than 19,000 years ago during the Last Glacial Maximum (LGM). Note that most of this melting occurred more than 6000 years ago, yet measurable velocities associated with this melting persist to the present time. Recently, Peltier et al. [31] and Argus et al. [3] introduced the ICE-6G\_C(VM5a) model that provides estimates for the present-day, GIA-related, 3-D crustal velocities associated with the melting of the LGM-related ice fields. For this study, the ICE-6G\_C(VM5a) vertical velocities (presented in Figure 8) were subtracted from their corresponding vertical velocities portrayed in Figure 6. Figure 9 presents the resulting vertical velocities. It will be helpful to use the vertical velocity field portrayed in Figure 9 for discussing how geophysical sources, other than GIA, influence the vertical motion found in Western CONUS.

The ICE-6G\_C(VM5a) model refers its velocities to the IGS08 reference frame, and so for their use in this study

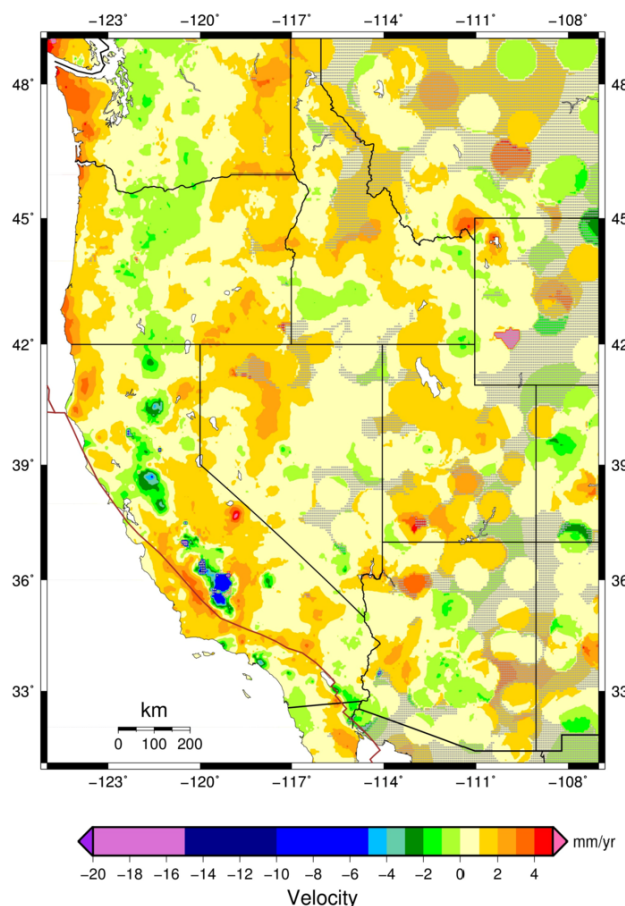


**Figure 9:** Estimated IGS14 vertical velocities after GIA-related motion has been removed. Gray screening identifies areas where increments to the vertical velocities from TRANS4D (version 0.1) have standard deviations exceeding 2.0 mm/yr.

these velocities were transformed into the IGS14 reference frame using transformation parameters published by Altamimi et al. [2]. The transformation from an IGS08 vertical velocity,  $V_{IGS08}$ , to its corresponding IGS14 vertical velocity,  $V_{IGS14}$ , involves seven transformation parameters. However, because five of these parameters equal zero, the transformation reduces to the equation

$$V_{IGS14} = V_{IGS08} + \dot{S} \times R + \dot{T}_Z \times (\sin \varphi) \quad (20)$$

where  $\dot{S} = -0.03 \times 10^{-9}/\text{yr}$  and  $\dot{T}_Z = 0.1 \text{ mm/yr}$ . In this equation,  $R (= 6.378 \times 10^9 \text{ mm})$  denotes Earth's radius and  $\varphi$  denotes the latitude associated with the velocity being transformed. Thus, for example, when  $\varphi = 40^\circ\text{N}$ , then

$$V_{IGS14} = V_{IGS08} - 0.13 \text{ mm/yr}. \quad (21)$$

According to ICE-6G\_C(VM5a), the IGS08 vertical components of these GIA-related velocities are between -2.0 mm/yr and 0.0 mm/yr almost everywhere throughout

Western CONUS (see Figure 8). Exceptions occur in parts of eastern Montana and northern Washington. In parts of eastern Montana some of the GIA-related IGS08 vertical velocities are between -3.0 mm/yr and -2.0 mm/yr and in parts of northern Washington they are between 0.0 mm/yr and 1.0 mm/yr. Figure 9 of this report presents the vertical velocity field that is obtained by subtracting the model-generated, GIA-related, vertical velocities (after they have been converted to IGS14) from the corresponding IGS14 vertical velocities that are presented in Figure 6. As revealed by Figure 9, most of Western CONUS is moving upward, except for relatively small patches of subsidence, after the present-day, vertical motion due to LGM-related GIA has been removed.

It should be mentioned that some uncertainty is associated with the GIA-related vertical velocities obtained using the ICE-6G\_C(VM5a) model. Snay et al. [37] estimated that this uncertainty is characterized by a standard deviation having an average value of 0.8 mm/yr worldwide. Local standard deviations may be lower or higher. Whatever the case, some of the uncertainty associated with the modeled GIA-related velocities should be added to the standard deviations presented in Figure 7 for properly interpreting the vertical velocities presented in Figure 9.

## 7 Discussion of resulting velocities

Recently, Hammond et al. [18] published a study of vertical velocities in California and Nevada. These authors employed GPS-derived velocities estimated by the University of Nevada, Reno using GPS data observed between 1996.0 and 2016.1. Furthermore, they refer their vertical velocities to the NA12 reference frame [7], which (according to Hammond et al.) can be transformed to corresponding IGS08 vertical velocities by adding approximately 0.67 mm/yr to the NA12 values. From Equation (21), it follows that NA12 vertical velocities are approximately 0.54 mm/yr lower than IGS14 velocities in California and Nevada. Hammond et al. [18] used a different interpolation method than that employed in this study. In particular, for estimating the vertical velocity at a specific location, Hammond et al. [18] calculated the weighted median of the observed vertical velocities at several “nearby” GPS stations. (In their study, a GPS station is “nearby” if it is connected to the location of interest by a line segment of the Delaunay triangulation involving this location and all of the GPS stations involved in their study. Also, their weights were based on an empirically derived function of distance.) Their approach has the effect of filtering

out velocity information from distant stations and filtering out velocity information from each station whose velocity varies greatly from the velocities of its neighboring stations. As a result, their velocity field and the velocity field of this study are usually similar in areas where the observed velocities are densely clustered, and the two velocity fields sometimes differ in areas where the observed velocities are sparsely clustered. A visual comparison of the two velocity fields may be performed by comparing Figure 6A of Hammond et al. [18] with Figure 6 of this report (keeping in mind that a  $\sim 0.54$  mm/yr bias exists between the respective reference frames).

In addition to estimating the vertical velocity field for California and Nevada, Hammond et al. [18] studied how a recent drought affected some of their results. In particular, much of Western CONUS experienced a severe drought for almost five years, from early 2011 until late 2015. Using GPS-derived velocities at sites located in the Sierra Nevada, these authors found that this area uplifted at rates between 0.5 and 1.0 mm/yr before 2011, whereas the same area uplifted at rates approximately twice as fast from 2011 to early 2016. This result reveals how temporal velocity variations limit the ability to produce a well-defined vertical velocity field. Nevertheless, some vertical velocity results for Western CONUS are discussed in the next several subsections. The discussions will necessarily be limited to areas having an adequate distribution of observed velocities as indicated by the diamonds and circles shown in Figure 2.

## 7.1 Subduction in the Pacific Northwest

Figure 9 shows that, in the absence of the motion associated with post-LGM GIA, the Pacific coastal areas of North America would be uplifting at rates from 0.0 to 5.0 mm/yr between latitudes  $41^{\circ}\text{N}$  and  $49^{\circ}\text{N}$ . This entire coastline experienced an M9.0 earthquake in the year 1700 [34]. This earthquake is associated with the subduction of the Juan de Fuca plate (and its neighbors, the Gorda plate to the south and the Explorer plate to the north) beneath the North America plate. Currently observed uplift rates corroborate the expectation that this coastal area can be expected to experience additional major earthquakes in the future. In the vicinity of the next earthquake, the resulting coseismic vertical displacement at a location is expected to be closely related to the total uplift to have accumulated at that location between 1700 and the time of the next large earthquake. Hence, the determination of accurate vertical velocities is critical for assessing the effects of future earthquakes that will occur in this coastal area.

Figure 9 further shows that uplift rates along the Pacific coast of northwestern CONUS are not spatially uniform. Indeed, after the GIA-related motion has been removed, coastal uplift rates are less than 2.0 mm/yr in central Oregon (approximately between latitudes  $43.5^{\circ}\text{N}$  and  $45^{\circ}\text{N}$ ), whereas corresponding coastal uplift rates exceed 2.0 mm/yr almost everywhere else between latitudes  $42^{\circ}\text{N}$  and  $49^{\circ}\text{N}$ . Burgette et al. [10] attributed this variation among the coastal uplift rates to a variation in the depth to which the interplate interface is locked. In particular, these authors have proposed that this interface is locked to a shallower depth between  $43.5^{\circ}\text{N}$  and  $45^{\circ}\text{N}$  than is the case elsewhere between  $42^{\circ}\text{N}$  and  $49^{\circ}\text{N}$ . Also, Figure 4A of McCaffrey et al. [25] shows that horizontal contraction rates are smaller along the coast of central Oregon than is the case along the remaining Pacific coast as far north as latitude  $50^{\circ}\text{N}$  and as far south as latitude  $42^{\circ}\text{N}$ . (Note that the study by McCaffrey et al. [25] did not include data that would allow them to estimate horizontal strain rates south of  $42^{\circ}\text{N}$ .) Thus, both the vertical and horizontal coseismic displacements associated with the next major earthquake on the interplate interface should be less along the central Oregon coast than they are at other Pacific Northwest coastal areas located to the north or south of central Oregon.

The direction of convergence of the subducting plates (Gorda, Juan de Fuca, and Explorer) relative to the North America plate varies (essentially monotonically) from ENE-ward in the southern extreme of the combined interplate boundary ( $\sim 40^{\circ}\text{N}$ ) to NE-ward in the northern extreme ( $\sim 50^{\circ}\text{N}$ ) as inferred from the direction of maximum contraction exhibited by the horizontal strain-rate estimates presented in Figure 4A of McCaffrey et al. [25]. Accordingly, vertical velocities generally decrease for some distance along the various paths from each point on the Pacific coast in the direction of plate convergence at that point. In most cases, velocities generally decrease over a distance exceeding 200 km along the corresponding path. In some cases, vertical velocities become negative (even after they have been corrected for GIA-related motion). Indeed, Figure 9 shows that several major subsidence patches reside in central Oregon and Washington, roughly between longitudes  $120^{\circ}\text{W}$  and  $123^{\circ}\text{W}$  and north of latitude  $41.5^{\circ}\text{N}$ . The subsidence occurring in this area may be down-warping resulting from the interplate collision. The influence of this collision within this subsidence area is corroborated by horizontal contraction rates (magnitude  $\approx 10^{-8}/\text{yr}$ ) occurring parallel to the direction of convergence (see Figure 4A of McCaffrey et al. [25]).

## 7.2 Pockets of significant subsidence

Even after removing GIA-related motion, several areas within Western CONUS are experiencing subsidence rates that exceed 3 mm/yr in magnitude (see Figure 9). The subsidence found in the vicinity of Lassen Peak (see Figure 1 for location) is associated with volcanism. The Lassen Peak area experienced significant eruptive activity starting in 1914 and continuing for several years [13]. According to Parker et al. [30], the current subsidence is likely related to horizontal extension, magma cooling, and/or fluid movement.

The other Western CONUS areas, where subsidence rates exceed 3 mm/yr in magnitude, exist as a result of groundwater extraction; and most of these areas are located in California's Central Valley. In this valley, water is critically needed to support agricultural activities. The water acquired via precipitation and/or its transport from surrounding areas is often insufficient. This insufficiency was especially the case during the regional drought that began in early 2011 and continued to late 2015. In many cases, the extraction of groundwater causes existing cavities within the aquifers to collapse. That is, water pressure within the aquifers had been sufficient to counterbalance the overburden pressure on these cavities until groundwater extraction reduced the water pressure below some critical value. When a cavity collapses, the associated subsidence is irreversible.

Unfortunately, the availability of repeated geodetic data in Western CONUS is woefully inadequate to accurately map the vertical motion associated with groundwater extraction. Repeated GNSS data provides relatively accurate vertical velocities (standard deviations < 1.0 mm/yr), but with poor spatial resolution (~10 km). Repeated satellite radar altimetry provides better spatial resolution (~1 km), but only for flat areas and with relatively inaccurate vertical velocities (standard deviations > 10 mm/yr). To make matters worse, the vertical motion associated with groundwater extraction often varies significantly over time because the amount of vertical motion is strongly related to the volume of groundwater that has been extracted and this volume varies over time in accordance with the need to supplement other available water resources by extracting groundwater. For the near future, it seems that interferometric synthetic aperture radar (InSAR) will provide the best available technology for mapping both the spatial and temporal variations associated with groundwater extraction. The report by Farr et al. [15] presents some interesting maps of vertical motion, which were produced by using repeated InSAR data observed in California between March 2015 and September 2016.

## 7.3 Areas of significant uplift

After removing GIA-related motion, several areas within Western CONUS are experiencing uplift rates that exceeds 3 mm/yr (see Figure 9). Some of these areas are located near the Pacific coast of North America between latitudes 41°N and 49°N. As previously discussed in Section 7.1, this uplift is associated with the subduction of the Juan de Fuca plate, together with the Gorda plate and the Explorer plate, beneath the North America plate. Hence, the following sections will address other areas of significant uplift.

### 7.3.1 Uplift associated with the Yellowstone Caldera

The Yellowstone Caldera sits above a mantle plume that is currently located beneath northwestern Wyoming, as shown in Figure 1. This caldera is the youngest in a series of progressively older silicic volcanic centers that extends southwestward for approximately 800 km along the Snake River Plain. This series of volcanic centers was formed as the North America plate drifted southwestwardly relative to the mantle plume at a rate of approximately 20 mm/yr. The Yellowstone Caldera itself was formed 634,000 years ago by a silicic eruption; and this caldera measures 45-km-wide by 75-km-long. Seismic tomographic imaging has revealed a chamber underlying the entire caldera from 8 to 16 km in depth. P-wave velocities within this chamber are low relative to such velocities in the surrounding crust. This chamber is thought to represent a hot, crystallizing magma system composed of partial melts and gases [23].

Vertical motion within the Yellowstone Caldera has been measured since 1923, first using leveling surveys, and more recently using GPS surveys and InSAR. The rates of vertical motion have varied significantly, both spatially and temporally, within the caldera. Figure 14 of Smith et al. [36] exhibits how an area within the Yellowstone Caldera, known as the Sour Creek resurgent domes, has moved vertically between 1923 and 2008. This area moved upward approximately 400 mm during these 85 years, which is equivalent to an average rate of 4.7 mm/yr. However, actual vertical rates have varied greatly over time. In particular, the average rate from 2004 to 2008 was on the order of 70 mm/yr, whereas the average rate from 1985 to 1995 was on the order of -16 mm/yr.

Additional details about the history of vertical motion in and around Yellowstone Caldera are provided by Vasco et al. [38], Chang et al. [12], and Smith et al. [36]. The temporal variations of this motion are thought to be related to the movement of magma and other fluids into and/or out from the aforementioned chamber. The vertical velocities

presented in Figures 6 and 9 merely represent temporally averaged rates that roughly corresponds to the 1995–2017 period.

### 7.3.2 Uplift associated with the Long Valley Caldera

Long Valley Caldera was formed by a colossal volcanic eruption 760,000 years ago. Located in eastern California (see Figure 1), this caldera measures approximately 32 km long (east-west) and 18 km wide (north-south). In May 1980, a strong earthquake swarm that included four M6 earthquakes struck the southern margin of this caldera associated with a 25-cm, dome-shaped uplift near the center of the caldera's floor. These events marked the onset of the latest period of caldera unrest that continues to this day. This ongoing unrest includes recurring earthquake swarms and continued dome-shaped uplift. No significant subsidence has yet to be observed within this caldera since 1980, which is in stark contrast to the Yellowstone Caldera where periods of uplift have been complemented with periods of subsidence. Additional information about the Long Valley Caldera are provided by Hill [21].

The uplift rates occurring in and around the center of Long Valley Caldera have varied over time with sharp increases following episodes of seismic swarms. Montgomery-Brown et al. [26] applied geodetic data to model the uplift that ensued after the occurrence of a seismic swarm in 2011. This uplift is well modeled by the inflation of a prolate spheroid magma reservoir located ~7 km beneath the resurgent dome. Their source model is consistent with source models associated with previous uplift episodes, suggesting the existence of a persistent reservoir. Gravity measurements performed between 1982 and 1998 detected an increase in mass within an assumed spherical source beneath the caldera floor. According to Battaglia et al. [4], this mass increase signifies that the inflation between 1982 and 1998 was likely due to intrusion of silicate magma, instead of either thermal expansion or hydrothermal pressurization. The vertical velocities presented in Figures 6 and 9 merely represent a temporally averaged rate that roughly corresponds to the 1995–2017 period.

### 7.3.3 Postseismic uplift near Hebgen Lake and elsewhere

In 1959, an M7.3 earthquake occurred near Hebgen Lake, Montana (see Figure 1 for location). Both Nashimura and

Thatcher [28, 29] and Chang et al. [11] had applied geodetic data to model the associated motion as viscoelastic relaxation within the lithosphere which followed this earthquake. These scientists, however, did not have access to newer results provided by nine years of continuous GPS observations at stations established near Hebgen Lake in 2008 as part of UNAVCO's Plate Boundary Observatory. The current results presented in Figure 9 reveal that an area, engulfing the faults that ruptured in 1959, is doming upward with rates exceeding 3 mm/yr near the center of this uplift dome after GIA-related motion has been removed.

Perhaps the high uplift rates occurring near Hebgen Lake represent more than lithospheric viscoelastic relaxation following the 1959 earthquake, otherwise these uplift rates would be expected to decrease monotonically as a function of time. Figure 12 of Smith et al. [36] indicates, however, that the rates of vertical motion near Hebgen Lake have varied significantly between 1987 and 2003. As discussed in Section 7.3.1, vertical motion within the Yellowstone Caldera may be attributed to this caldera's location above a mantle plume. Because Hebgen Lake is located approximately 25 km northwest of a point on the rim that encircles the Yellowstone Caldera, the temporal variation in vertical motion occurring near Hebgen Lake most likely relates to its proximity to the Yellowstone Caldera.

Certainly, such postseismic motion is also occurring near other major earthquakes that have occurred east of the San Andreas Fault System. In particular, Hammond et al. [18] discuss postseismic uplift associated with earthquakes that have occurred in the Central Nevada Seismic Belt (including the 1915 M7.2 Pleasant Valley earthquake and the 1954 M7.1 Fairview Peak earthquake) and with earthquakes that occurred in the Eastern California Shear Zone (including the 1992 M7.3 Landers earthquake and the 1999 M7.1 Hector Mine earthquake). According to Figure 9, the current postseismic uplift rate near each of these other earthquakes is less than 3 mm/yr, after GIA-related motion has been removed (see Figure 1 for earthquake locations).

### 7.3.4 Uplift along the San Andreas Fault System

Figure 9 reveals that uplift is occurring almost everywhere within a ~20-km-wide strip that engulfs the San Andreas Fault System (SAFS) between latitudes 33.5°N and 36.5°N. In particular, these uplift rates exceed 3 mm/yr between latitudes 35.5°N and 36.0°N. Howell et al. [22] suggest that the uplift near the SAFS results primarily from a combination of two physical phenomena: (1) the lithospheric flexure associated with an elastic layer overlying a viscoelas-

tic substrate together and with the fault geometry and the slip variations (both spatial and temporal) associated with the SAWS, and (2) long wavelength isostasy associated with groundwater extraction.

Regarding the lithospheric flexure, Howell et al. [22] developed a physical model representing vertical velocities within the rectangle bounded by latitudes 32°N and 36°N and longitudes 115°W and 121°W. Their model represents regional vertical motion due to the interaction among creeping and locked faults within a 50-km-thick elastic plate overlaying an asthenosphere having a viscosity of  $1 \times 10^{19}$  Pa s. They found that their physical model reflected the vertical velocity pattern deduced from GPS data after removing some highly uncertain data and some effects caused by other physical phenomena. Perhaps the most dominant of these removed effects is associated with groundwater extraction at locations within ~100 km of the SAWS. As discussed in Section 7.2 of this report, groundwater extraction produces subsidence within the immediate vicinity of the locations where the extraction is occurring. However, this extraction also produces some uplift both in this immediate vicinity and in its surroundings because the gravitational burden of the water is being redistributed, especially with much of the extracted water eventually evaporating into the atmosphere. Thus, in the immediate vicinity of groundwater extraction, the net effect of this extraction is subsidence, but further away the net effect is uplift. Figure 13b of Hammond et al. [18] presents a model of the uplift associated with recent groundwater extraction in the area surrounding California's Central Valley. Unfortunately, associated uplift rates will vary temporally because rates of groundwater extraction vary temporally. Thus, the high uplift rates found along parts of the SAWS, as seen in Figure 9, may be inflated due to the recent California drought and the resulting need to extract higher-than-usual amounts of groundwater within California's Central Valley. See also Borsa et al. [9] for a discussion of drought-induced uplift in the western United States.

## 8 Summary

Version 0.2 of the TRANS4D software has been developed. As compared to version 0.1, this newer version incorporates an improved model for the vertical velocity field of Western CONUS thanks to the availability of additional geodetic data and the application of a new modeling process. The new data provide estimates of vertical velocities at approximately 1300 additional geodetic stations,

including 598 leveling stations located near the Pacific coast of Oregon and northern California and 690 satellite radar altimetry stations located in California's Central Valley. Also, the new data provide vertical velocities spanning longer time intervals at some previously employed GNSS stations. In particular, this study includes some GNSS data observed as recently as mid-2017, whereas all of the GNSS data used to create version 0.1 were observed in 2013 or earlier.

The new modeling process involves two steps. The first step involves adopting a preliminary model and computing velocity residuals by subtracting model velocities from corresponding "observed" velocities. For this study, the vertical velocity model from TRANS4D (version 0.1) serves as the preliminary model. The second step involves interpolating the residual velocities to estimate incremental velocities at the nodes of a 2-D grid having a spacing of  $0.0625^\circ \times 0.0625^\circ$  in latitude and longitude. These incremental velocities were then added to corresponding velocities of the preliminary model to obtain the "final" velocities at the grid nodes. The final velocities at other locations within the grid may then be determined via bilinear interpolation of the final grid-node velocities as is encoded in the TRANS4D software. Consequently, version 0.2 provides significantly better spatial resolution of Western CONUS's vertical velocity field than does version 0.1, which is based on a grid having a node spacing of  $0.25^\circ \times 0.25^\circ$  in latitude and longitude. As is inevitable, additional information/data and improved estimation processes will eventually become available, and the current "final" velocities may become preliminary velocities for determining even more accurate "final" velocities.

To better understand the newly estimated vertical velocity field of Western CONUS, that component of this velocity field which is due to the GIA associated with past melting of the ice fields that formed during the Last Glacial Maximum was removed using the ICE-6G\_C(VM5a) model of Peltier et al. [31] and Argus et al. [3]. The resulting vertical velocity field (Figure 9) provides several insights into some geophysical processes occurring in Western CONUS. The large scale geophysical processes, that involve vertical velocities having magnitudes in excess of 3 mm/yr (after removing GIA-related velocities), include subduction in the Pacific Northwest, uplift along the San Andreas Fault System, and subsidence due to groundwater extraction in California's Central Valley. The small scale geophysical processes, which involve vertical velocities having magnitudes in excess of 3 mm/yr (after removing GIA-related velocities), include subsidence at Lassen Peak Volcano and uplift at both the Yellowstone Caldera and the Long Valley Caldera. Also, uplift rates exceeding 3 mm/yr (after

removing GIA-related velocities) are currently occurring near Hebgen Lake where an M7.3 earthquake occurred in 1959. The fact that vertical velocities for most of these geophysical processes experience temporal variations makes it difficult to accurately model them. While removing the model-generated velocities associated with GIA is helpful for understanding the influence of other geophysical phenomena on the observable vertical velocity field, the TRANS4D software provides its users with estimates for only the observable vertical velocity field, that is, the velocity field presented in Figure 6.

**Acknowledgments:** The authors thank the many people and institutions that were involved in collecting and/or processing the geodetic data involved in this study; most notably the authors thank Cheinway Hwang and his colleagues who provided the satellite altimetry data. The authors also thank William Hammond, Jacob Heck, Stephen Hiller, Scott Martin, Jim Ray, Tomás Soler, and an anonymous reviewer for suggestions that improved the presentation of this paper. The figures have been created using Generic Mapping Tools [39]. This research was sponsored in part by NOAA's National Geodetic Survey. The supporting information associated with this paper (Data\_Set\_S1.txt) provides the stage-2 velocities that were estimated for approximately 12,500 geodetic reference stations involved in this study.

## Appendix A. Combining vertical velocities obtained from leveling data with GNSS-derived vertical velocities

GNSS data yield what are referred to as ellipsoid heights. The ellipsoid height,  $h(\varphi, \lambda, t)$ , at a point having latitude  $\varphi$ , longitude  $\lambda$ , and at time  $t$  is the geometric height of this point above (or below) a specified ellipsoid of revolution whose geometric center coincides with the origin of a given 3-D Cartesian reference frame (such as IGS14) and whose axis of rotation corresponds to the Z-axis of this reference frame. The specification of the ellipsoid of revolution is accomplished by selecting two parameters that define its size and shape (for example, the lengths of its semi-major axis and its semi-minor axis). In the TRANS4D software, the specified ellipsoid of revolution equals that adopted for defining the Geodetic Reference System of 1980 [27]. The magnitude of the desired ellipsoid height at a point equals the distance from this point to the ellipsoidal sur-

face along a straight line that pierces the ellipsoidal surface at latitude  $\varphi$  and longitude  $\lambda$  in such a way that this line is normal to the ellipsoidal surface at the pierce point. The ellipsoid height is positive if the point lies outside of the ellipsoidal surface, and negative if it lies inside, otherwise the height is zero. In accordance with the above definition of ellipsoid height, repeated GNSS data collected at latitude  $\varphi$  and longitude  $\lambda$  yield the ellipsoidal vertical velocity  $V_h(\varphi, \lambda)$  defined by the equation

$$V_h(\varphi, \lambda) = dh(\varphi, \lambda, t)/dt. \quad (\text{A1})$$

This velocity is geometric in nature in that it is independent of spatial variations in Earth's gravity field. (Note: The orbital paths of GNSS satellites are influenced by spatial variations in Earth's gravity field, but this influence is mathematically removed when processing GNSS data to obtain ellipsoid heights.)

On the other hand, leveling data yield what are referred to as orthometric heights. The orthometric height,  $H(\varphi, \lambda, t)$ , at a point having latitude  $\varphi$ , longitude  $\lambda$ , and at time  $t$  equals the distance from this point along the curved plumb line through this point which pierces a specified realization of the geoid at latitude  $\varphi$  and longitude  $\lambda$ . The orthometric height is positive if the point lies outside of the geoid and negative if it lies inside, otherwise it is zero. In accordance with the above definition of orthometric height, repeated leveling data collected at latitude  $\varphi$  and longitude  $\lambda$  yield the orthometric vertical velocity  $V_H(\varphi, \lambda)$  defined by the equation

$$V_H(\varphi, \lambda) = dH(\varphi, \lambda, t)/dt. \quad (\text{A2})$$

The relationship between ellipsoid heights and orthometric heights is frequently approximated by the expression:

$$h(\varphi, \lambda, t) \approx H(\varphi, \lambda, t) + N(\varphi, \lambda, t) \quad (\text{A3})$$

where  $N(\varphi, \lambda, t)$  denotes the geoid height, that is, the distance of the geoid above (positive) or below (negative) the reference ellipsoid at latitude  $\varphi$  and longitude  $\lambda$  and at time  $t$ . Consequently,

$$V_h(\varphi, \lambda) \approx V_H(\varphi, \lambda) + V_N(\varphi, \lambda), \quad (\text{A4})$$

where  $V_N(\varphi, \lambda) = dN(\varphi, \lambda, t)/dt$ . In essence,  $V_N(\varphi, \lambda)$  measures the vertical velocity of the geoid at latitude  $\varphi$  and longitude  $\lambda$ . This velocity is related to temporal changes in Earth's gravity field. While this velocity is currently being measured by certain Earth-orbiting satellites, such as those associated with NASA's Gravity Recovery and Climate Experiment (GRACE), the resulting spatial resolution of  $V_N(\varphi, \lambda)$  exceeds 100 kilometers. Thus, it will be assumed that  $V_N(\varphi, \lambda)$  is constant over the

spatial extent of the leveling surveys involved in this study.

An additional concern, involved when dealing with leveling data, is that an individual leveling survey can provide only differences in orthometric heights among two or more points. That is, an individual leveling survey, by itself, cannot provide the orthometric height of any individual point. It follows that repeated leveling surveys cannot provide the orthometric vertical velocity of any individual point. Thus, it is necessary to provide the orthometric vertical velocity for one or more points contained in the leveling network to obtain orthometric vertical velocities at other points from repeated leveling surveys. Burgette et al. [10] accomplished this by using the relative rate of sea level change measured at six tide gauges in combination with an estimated absolute rate of sea level change for their study area. The relative rate of sea level change at a tide gauge equals the rate of sea level change relative to a specified geodetic reference station located near the tide gauge. For a specified area, the absolute rate of sea level change equals the estimated average rate of sea level change relative to Earth's center for that area. Hence, the difference (absolute rate minus relative rate) at a given tide gauge provides an estimate of the orthometric vertical velocity at the geodetic reference station associated with this tide gauge. Moreover, the reference stations associated with these six tide gauges are part of the repeatedly surveyed leveling network being considered. For their study, Burgette et al. estimated the absolute rate of sea level change along the coast of Oregon and northern California to equal 2.28 mm/yr during the 1925–2006 interval of time. The accuracy of their estimated orthometric vertical velocity at each of the 598 geodetic reference stations relies on the accuracy of this estimated value.

For the study being reported in this publication, the 598 orthometric vertical velocities estimated by Burgette et al. were compared with corresponding IGS14 ellipsoid vertical velocities obtained from repeated GNSS data. This comparison involved interpolating ellipsoid velocities from the GNSS sites to the 598 leveling sites. The results indicate that the orthometric vertical velocities derived from leveling data by Burgette et al. are, on average,  $1.04 \pm 0.03$  mm/yr higher than the interpolated ellipsoid vertical velocities based on the GNSS data. Consequently, the orthometric vertical velocities of Burgette et al. were each decreased by 1.04 mm/yr to produce the corresponding ellipsoidal vertical velocities used in this study. This difference is, in part, an expected difference between orthometric vertical velocities and ellipsoidal vertical velocities, in accordance with Equation (A4). Additionally, this difference may reflect an error in the value of the absolute

rate of sea level change used by Burgette et al. or an error related to the interpolation of GNSS-derived ellipsoid velocities to leveling-derived orthometric velocities. Furthermore, this difference may reflect that the rate of absolute sea level change does not equate to  $V_N(\varphi, \lambda)$ . That is, both  $V_N(\varphi, \lambda)$  and the rate of absolute sea level change relate similarly to the rate of gravity change, but  $V_N(\varphi, \lambda)$  and the rate of absolute sea level change relate differently to changes in water volume (due to temperature variations) and to the redistribution of water (such as that associated with the melting of glaciers).

## References

- [1] Altamimi, Z., Collilieux, X., & Metivier, L. (2011). ITRF2008: an improved solution of the International Terrestrial Reference Frame. *Journal of Geodesy*, 85(8), 457–473. <https://doi.org/10.1007/s00190-011-0444-4>.
- [2] Altamimi, Z., Rebischung, P., Metivier, L., & Collilieux, X. (2016). ITRF2014: A new release of the International Terrestrial Reference Frame modeling non-linear station motions. *Journal of Geophysical Research: Solid Earth*, 121, 6109–6131. <https://doi.org/10.1002/2016JB013098>.
- [3] Argus, D. F., Peltier, W. R., Drummond, R., & Moore, A. W. (2014). The Antarctica component of postglacial rebound model ICE-6G\_C(VM5A) based upon GPS positioning, exposure age dating of ice thickness, and relative sea level histories. *Geophysical Journal International*, 198(1), 537–563. <https://doi.org/10.1093/gji/ggu140>.
- [4] Battaglia, M., Segall, P., & Roberts, C. (2003). The mechanics of unrest at Long Valley Caldera, California. 2. Constraining the nature of the source using geodetic and micro-gravity data. *Journal of Volcanology and Geothermal Research*, 123, 219–245.
- [5] Blewitt, G., et al. (2005). A stable North American reference frame (SNARF): First release. Working Group Report, UNAVCO, Boulder, Colorado [Available at <https://www.unavco.org/projects/past-projects/snarf/SNARF1.0/SNARF1.0.html>, last accessed 12 September 2017].
- [6] Blewitt, G., Kreemer, C., Hammond, W. C., & Gazeaux, J. (2016). MIDAS robust trend estimator for accurate GPS station velocities without step detection. *Journal of Geophysical Research: Solid Earth*, 121, 2054–2068. <https://doi.org/10.1002/2015JB012552>.
- [7] Blewitt, G., Kreemer, C., Hammond, W. C., & Goldfarb, J. M. (2013). Terrestrial reference frame NA12 for crustal deformation studies in North America. *Journal of Geodynamics*, 72, 11–24. <https://doi.org/10.1016/j.jog.2013.08.004>.
- [8] Bock, Y., & Webb, F. (2012). MEASUREs Solid Earth Science ESDR System. La Jolla, California and Pasadena, California, USA. <http://sopac-ftp.ucsd.edu/pub/timeseries/measures/timeseriesModelTermsSummary.MEASUREs Combination.20130627.txt>.
- [9] Borsa, A. A., Agnew, D. C., & Cayan, D. R. (2014). Ongoing drought-induced uplift in the western United States. *Science*, 345(6204), 1587–1590.

- [10] Burgette, R. J., Weldon II, R. J., & Schmidt, D. A. (2009). Interseismic uplift rates for western Oregon and along-strike variation in locking on the Cascadia subduction zone. *Journal of Geophysical Research*, 114, B01408. <https://doi.org/10.1029/2008JB005679>.
- [11] Chang, W.-L., Smith, R. B., & Puskas, C. M. (2013). Effects of lithospheric viscoelastic relaxation on the contemporary deformation following the 1959  $M_W$  7.3 Hebgen Lake, Montana, earthquake and other areas of the intermountain seismic belt. *Geochemistry, Geophysics, Geosystems*, 14. <https://doi.org/10.1029/2012GC004424>.
- [12] Chang, W.-L., Smith, R. B., Wicks, C., Puskas, C., & Farrell, J. (2007). Accelerated uplift and some source models of the Yellowstone Caldera, 2004–2006, from GPS and InSAR observations. *Science*, 318(5852), 952–956. <https://doi.org/10.1126/science.1146842>.
- [13] Clyne, M. A., Christiansen, R. L., Felger, T. J., Stauffer, P. H., & Hendley, J. W. (1999). Eruptions of Lassen Peak, California, 1914 to 1917. U.S. Geological Survey Fact Sheet, 172-98, 2. [Available at <http://pubs.usgs.gov/fs/1998/fs173-98/> last accessed 12 September 2017].
- [14] Craymer, M. R., Henton, J. A., Piraszewski, M., & Lapelle, E. (2011). An updated GPS velocity field for Canada. Abstract G21A-0793, presented at 2011 Fall Meeting, American Geophysical Union, San Francisco, Calif., 5–9 Dec.
- [15] Farr, T. G., Jones, C. E., & Liu, Z. (2017). Progress report: Subsidence in California, March 2015 – September 2016 [Report prepared for California Department of Water Resources, available at <http://water.ca.gov> (access by entering paper's title into this website's search utility), last accessed 12 September 2017].
- [16] Goovaerts, P. (1997). *Geostatistics for Natural Resources Evaluation*, Oxford University Press, ISBN 0-19-511538-4.
- [17] Griffiths, J., Rohde, J. R., Cline, M., Dulaney, R. L., Hilla, S., Kass, W. G., ... Soler, T. (2010). Reanalysis of GPS data for a large and dense regional network tied to a global reference frame. IAG Commission 1 Symposium 2010, Reference Frames for Applications in Geosciences (REFAG2010), Marne-La-Vallée, France, October 4–8.
- [18] Hammond, W. C., Blewitt, G., & Kreemer, C. (2016). GPS imaging of vertical land motion in California and Nevada: Implication for Sierra Nevada uplift. *Journal of Geophysical Research: Solid Earth*, 121. <https://doi.org/10.1002/2016JB013458>.
- [19] Herring, T., Craymer, M., Sella, G., Snay, R., Blewitt, G., Argus, D., ... Tamasia, M. (2008). SNARF 2.0: A regional reference frame for North America. *EOS Transactions of the American Geophysical Union*, 89, Joint Assembly Suppl., Abstract G12B-01.
- [20] Herring, T. A., Melbourne, T. I., Murray, M. H., Floyd, M. A., Szeliga, W. M., King, R. W., ... Wang, L. (2016). Plate Boundary Observatory and related networks: GPS data analysis methods and geodetic products. *Reviews of Geophysics*, 54. <https://doi.org/10.1002/2016RG000529>.
- [21] Hill, D. (2006). Unrest in Long Valley Caldera, California, 1978–2004. Mechanics of Activity and Unrest at Long Valley Caldera, edited by C. Troise, G. DeNatali, and C. R. Kilburn, *Geological Society London Special Publication*, 269, 1–24.
- [22] Howell, S. M., Smith-Konter, B., Frazer, N., Tong, X., & Sandwell, D. (2016). The vertical fingerprint of earthquake cycle loading in southern California. *Nature Geoscience*. <https://doi.org/10.1038/ngeo2741>.
- [23] Husen, S., Smith, R. B., & Waite, G. P. (2004). Evidence for gas and magmatic sources beneath the Yellowstone volcanic field from seismic tomographic imaging. *Journal of Volcanology and Geothermal Research*, 131, 397–410. [https://doi.org/10.1016/s/377-0273\(03\)00416-5](https://doi.org/10.1016/s/377-0273(03)00416-5).
- [24] Hwang, C., Kao, R., Han, J., Shum, C. K., Galloway, D. L., Sneed, M., ... Li, F. (2016). Time-varying land subsidence detected by radar altimetry: California, Taiwan and north China. *Scientific Reports*, 6, 28160. <https://doi.org/10.1038/srep28160>, [www.nature.com/scientificreports/](http://www.nature.com/scientificreports/).
- [25] McCaffrey, R., King, R. W., Payne, S. J., & Lancaster, M. (2013). Active tectonics of northwestern U.S. inferred from GPS-derived surface velocities, *Journal of Geophysical Research: Solid Earth*, 118. <https://doi.org/10.1029/2012JB009473>.
- [26] Montgomery-Brown, E. K., Wicks, C. W., Cervelli, P. F., Langbein, J. O., Svarc, J. L., Shelley, D. R., ... Lisowski, M. (2015). Renewed inflation of Long Valley Caldera, California (2011 to 2014). *Geophysical Research Letters*, 42, 5250–5257. <https://doi.org/10.1002/2015GL064338>.
- [27] Moritz, H. (1984). Geodetic Reference System 1980, *Bulletin Géodésique*, 54(3), 388–398.
- [28] Nashimura, T., & Thatcher, W. (2003). Rheology of the lithosphere inferred from postseismic uplift following the 1959 Hebgen Lake earthquake. *Journal of Geophysical Research*, 108. <https://doi.org/10.1029/2002JB002191>.
- [29] Nashimura, T., & Thatcher, W. (2004). Correction to “Rheology of the lithosphere inferred from postseismic uplift following the 1959 Hebgen Lake earthquake”. *Journal of Geophysical Research*, 109. <https://doi.org/10.1029/2003JB002798>.
- [30] Parker, A. L., Biggs, J., & Lu, Z. (2016). Time-scale and mechanism of Lassen Volcanic Center, CA from InSAR. *Journal of Volcanology and Geothermal Research*, 320, 117–127.
- [31] Peltier, W. R., Argus, D. F., & Drummond, R. (2015). Space geodesy constrains ice age terminal deglaciation: The global ICE-6G\_C(VM5A) model. *Journal of Geophysical Research: Solid Earth*, 120, 450–487. <https://doi.org/10.1002/2014JB011176>.
- [32] Rebischung, P., Altamimi, Z., Ray, J., & Garayt, B. (2016). The IGS contribution to ITRF2014. *Journal of Geodesy*. <https://doi.org/10.1007/s00190-016-0897-6>.
- [33] Rebischung, P., Griffiths, J., Ray, J., Schmid, R., Collilieux, X., & Garayt, B. (2012). IGS08: The IGS realization of ITRF2008, *GPS Solutions*, 16, 483–494. <https://doi.org/10.1007/s10291-011-0242-2>.
- [34] Satake, K., Wang, K., & Atwater, B. F. (2003). Fault slip and seismic moment of the 1700 Cascadia earthquake inferred from the Japanese tsunami descriptions. *Journal of Geophysical Research*, 108, B11. <https://doi.org/10.1029/2003JB002521>.
- [35] Shen, Z.-K., King, R. W., Agnew, D. C., Wang, M., Herring, T. A., Dong, D., & Fang, F. (2011). A unified analysis of crustal motion in southern California, 1970–2004: The SCEC crustal motion map. *Journal of Geophysical Research*, 116, B11402. <https://doi.org/10.1029/2011JB008549>.
- [36] Smith, R. B., Jordan, M., Steinberger, B., Puskas, C. M., Farrell, J., Waite, G. P., ... O'Connell, R. (2009). Geodynamics of the Yellowstone hotspot and mantle plume: Seismic and GPS imaging, kinematics, and mantle flow. *Journal*

- of Volcanology and Geothermal Research, 188, 26–56, <https://doi.org/10.1016/j.volgeores.2009.08.020>.
- [37] Snay, R. A., Freymueller, J. T., Craymer, M. R., Pearson, C. F., & Saleh, J. (2016). Modeling 3-D crustal velocities in the United States and Canada. *Journal of Geophysical Research: Solid Earth*, 121, 5365–5388. <https://doi.org/10.1002/2016JB012884>.
- [38] Vasco, D. W., Puskas, C. M., Smith, R. B., & Meertens, C. M. (2007). Crustal deformation and source models of the Yellowstone volcanic field from geodetic data. *Journal of Geophysical Research*, 112, B07402. <https://doi.org/10.1029/2006JB004641>.
- [39] Wessel, P., & Smith, W. H. F. (1998). New improved version of generic mapping tools released, *Eos Transaction of the American Geophysical Union*, 79(47), 579. <https://doi.org/10.1029/98EO00426>.

---

**Supplemental Material:** The online version of this article offers supplementary material (<https://doi.org/10.1515/jag-2018-0010>). This supplementary material is in the form of a data file that provides 3-D crustal velocities for approximately 12,500 geodetic stations distributed around the world. These velocities were derived from the nine data sets described in Section 2.1 of this article using the combination process discussed in Section 2.1.